Climate Dynamics (2026) 64:230
https://doi.org/10.1007/s00382-026-08199-9

Late-spring rainfall over East Asia linked to variability in the Tibetan Plateau vortex street-like system

Ruyu Gan[1,2] · Gang Huang[2,3]

Received: 15 September 2025 / Accepted: 15 April 2026

Abstract

Late-spring precipitation variability over East Asia has important implications for public safety, agriculture, and regional socioeconomic systems. A vortex street-like system east of the Tibetan Plateau (TPVSL) is known to shape extreme summer rainfall, yet its influence on spring precipitation remains unclear. Using daily reanalysis together with CHIRPS-2.0 satellite–gauge blended precipitation data and CPC gauge-based observations, we investigate the influence of strong and weak TPVSL events on May precipitation over East Asia. TPVSL-related cyclonic activity accounts for more than 80% of total rainfall across much of eastern China and exceeds 95% in core regions. Variations in TPVSL intensity are significantly correlated with May precipitation across East Asia. Intensified TPVSL activity is associated with stronger upstream westerlies south of the Tibetan Plateau, while downstream westerlies help maintain a stable propagation latitude. Satellite–gauge and gauge-based datasets provide consistent evidence of the TPVSL–rainfall relationship. TPVSL variability enhances upward motion and moisture transport along its propagation pathway, thereby promoting extreme May precipitation across East Asia. Monitoring TPVSL intensity and position may therefore improve flood forecasting and climate prediction of East Asian precipitation.

Keywords Southwest China vortex · Vortex street-like system · Tibetan plateau · Late-spring rainfall · East China · Japan and Korea

1 Introduction

In recent years, East Asia has experienced destructive rainfall events in May, including those in 2021 and 2025, which caused severe flooding and substantial societal disruption. In contrast, some years have also been characterized by pronounced precipitation deficits, such as the widespread rainfall shortage observed in 2007. These contrasting anomalies highlight the pronounced variability of May rainfall across East Asia and its profound implications for both natural ecosystems and socioeconomic activities. As May typically marks the onset of the rainy season, excessive precipitation substantially increases disaster risk. For example, heavy rainfall in provinces such as Guizhou and Guangxi has triggered floods and landslides, leading to loss of life and property damage (Ombadi et al. 2023; Wu et al. 2024). From an agricultural perspective, May coincides with the early growth stage of key crops. Excessive rainfall can waterlog soils, hinder sowing and germination, and promote the spread of pests and diseases, thereby threatening agricultural production (Han et al. 2024; Kim et al. 2024).

Spring precipitation anomalies over East Asia are strongly modulated by the East Asian monsoon circulation system, including the East Asian westerly jet and the Western Pacific Subtropical High (WPSH). Variations in the position and strength of the westerly jet affect vertical motion conditions and thus influence spring rainfall across East Asia (Huang et al. 2015; Xie et al. 2015; Wang et al. 2021). Changes in the intensity and location of the WPSH regulate moisture pathways and ascending motion, exerting a significant impact

✉ Ruyu Gan
ganry@just.edu.cn

✉ Gang Huang
hg@mail.iap.ac.cn

1 Ocean College, Jiangsu University of Science and Technology, Zhenjiang, China

2 State Key Laboratory of Earth System Numerical Modeling and Application, Institute of Atmospheric Physics, Chinese Academy of Sciences, Beijing, China

3 University of Chinese Academy of Sciences, Beijing, China

Published online: 19 May 2026

on spring precipitation over the region (Gu et al. 2021; Jia et al. 2021). In addition to large-scale circulation anomalies, sea surface temperature anomalies also exert a critical influence on spring precipitation over East Asia, including those in the Pacific (Wu et al. 2003; Feng and Li 2011; Gu et al. 2018), Indian (Yang and Lau 2004; Xie et al. 2020), and Atlantic Oceans (You and Jia 2018; Jia et al. 2019). During the mature phase of El Niño, warming in the central–eastern Pacific and tropical Indian Ocean excites a western North Pacific anticyclone that can persist into the following summer through the "capacitor effect" and local air–sea feedbacks (Wang et al. 2000; Xie et al. 2009), thereby increasing spring rainfall over South China (Zhang and Sumi 2002). Wintertime SST anomalies in the Indian Ocean also exert a strong influence on East Asian rainfall. For example, negative SST anomalies over the southern Indian Ocean can weaken and retreat the WPSH eastward, while enhancing anomalous meridional overturning circulation and vertical ascent, which ultimately increases late-spring rainfall over South China (Jia et al. 2021).

Beyond these large-scale factors, orographically induced vortex systems also exert a pronounced influence. Southwest vortices and lee cyclones east of the Tibetan Plateau frequently propagate eastward, shaping rainfall over Southwest China and downstream regions (Fu et al. 2015, 2016; Curio et al. 2019; Li et al. 2021). Their interaction with the Plateau's complex terrain and with low-level southerly flows provides a key sustaining mechanism for persistent spring rains (Wan and Wu 2007).

Notably, previous and recent studies have identified a vortex street-like system in the wake of the Tibetan Plateau, referred to as the Tibetan Plateau Vortex Street-Like (TPVSL) system, which has long been recognized as an important textbook phenomenon (Yeh 1950). Observations indicate that the westerlies often form vortex street patterns as they flow around the Plateau (Yeh and Gao 1979; Ding 1992; Wu 1999; Huang and Zhou 2004). Wu identified structural similarities between the East Asian circulation and the classical Kármán vortex street, noting that the Southwest China Vortex and the Lanzhou Small High correspond to the southern and northern branches, respectively (Wu 1999). Building on this concept, Liu et al. (2023) quantitatively demonstrated the parametric consistency between this structure and laboratory-modeled Kármán vortex streets, naming it the Tibetan Plateau Vortex Street-Like (TPVSL) system. Cyclonic components within the TPVSL provide favorable conditions for precipitation development, suggesting that the system may serve as a key organizing mechanism of the East Asian rainband. The propagation of the TPVSL is primarily controlled by the downstream westerlies and the northern boundary of the WPSH.

Based on this framework, Liu et al. (2025) analyzed two extreme rainfall events in eastern China in June–July 2020 and 2024. They showed that TPVSL anomalies convincingly explained these events and clarified how surrounding circulation systems modulated precipitation through their influence on the vortex street. The presence of the TPVSL and its significant climatic role over East Asia were also identified in simulations with the ACCESS-ESM1—5 model (Liu et al. 2025). Furthermore, the circulation structure east of the Plateau closely resembles fluid dynamics experiments at Reynolds numbers on the order of 10^4 (Khan et al. 2017; Son et al. 2020; Anwar et al. 2022).

Here we investigate whether the TPVSL also exerts a central influence on May rainfall anomalies. Building on the framework of Liu et al. (2025), which focused on extreme summer rainfall over eastern China, this study examines whether the TPVSL mechanism extends to late-spring conditions and explores the contrasting impacts of strong and weak TPVSL regimes. The analysis further expands the spatial domain to East Asia, including the Korean Peninsula and Japan, and evaluates the robustness of the TPVSL–rainfall relationship using both CHIRPS satellite–gauge data and CPC gauge observations.

The remainder of this paper is organized as follows. Section 2 introduces the data and methods. Section 3 presents the distinct characteristics of the two TPVSL regimes (strong TPVSL and weak TPVSL), quantifies their respective contributions to precipitation variability, and examines their anomalous features with an emphasis on positional changes, intensity, and interactions with surrounding circulation systems. Section 4 discusses the broader implications and concludes the study.

1.1 Data

Daily precipitation data are obtained from both satellite-derived and gauge-based datasets. The satellite product is CHIRPS-2.0 (Climate Hazards Group InfraRed Precipitation with Station Data; https://data.chc.ucsb.edu), a high-r esolution satellite–gauge blended dataset developed for the Famine Early Warning Systems Network (FEWS NET). CHIRPS combines infrared satellite precipitation estimates with in situ rain-gauge observations and provides daily precipitation at $0.05° \times 0.05°$ spatial resolution from 1 January 1981 to 31 July 2025 (Funk et al. 2015). Gauge-based precipitation data are obtained from the Climate Prediction Center (CPC) Global Unified Gauge-Based Analysis of Daily Precipitation (Chen et al. 2008), a $0.5° \times 0.5°$ gridded dataset available from 1979 to the present. To maintain consistency with CHIRPS, the analysis period is limited to 1 January 1981 to 31 July 2025. Analyses are primarily based on CHIRPS and CPC, and the main conclusions are not sensitive to the choice of dataset.

Daily horizontal wind fields are obtained from two reanalysis products: the National Centers for Environmental Prediction/National Center for Atmospheric Research (NCEP/NCAR) Reanalysis (Kalnay et al. 1996) and the European Centre for Medium-Range Weather Forecasts Reanalysis version 5 (ERA5) (Hersbach et al. 2020). The variables analyzed include daily zonal and meridional wind components at 700 hPa and daily zonal wind at 200 hPa. Both datasets are interpolated onto a common 0.5° grid for the period 1981 to 2025. Previous studies have shown that these reanalyses adequately capture vortex activity (Curio et al. 2019) and the structure of the vortex street-like system east of the Tibetan Plateau (Liu et al. 2023, 2025). The analysis domain is defined based on the climatological May precipitation band and represented as a southwest–northeast-oriented parallelogram with vertices at (24°N, 107°E), (31°N, 107°E), (34°N, 140°E), and (41°N, 140°E).

To evaluate whether climate models reproduce the observed TPVSL characteristics, historical simulations from the ACCESS-ESM1—5 model (r1i1p1f1) within the CMIP6 framework (O'Neill et al. 2016) are also analyzed. The simulation spans from 1 January 1950 to 31 December 2014.

Following Kong and Chiang (2020), the latitudinal position of the westerly jet is defined using the 200-hPa zonal wind field. The zonal mean wind across the longitudinal sector 80°–100°E is first calculated, and the latitude of the maximum zonal wind within 20°–50°N is identified as the jet axis skirting the Tibetan Plateau. This latitude range is chosen to avoid potential confusion with the polar front jet, which is typically located at higher latitudes.

1.2 Identification of the vortex street structure and related metrics

Daily relative vorticity fields with a horizontal resolution of 2.5° × 2.5° are used to characterize the TPVSL. This resolution is sufficient to resolve the dominant scales of the vortex street over East Asia, which typically exhibits a zonal spacing of approximately 2,000 km and a meridional separation of about 1,000 km between the northern and southern branches. These scales correspond to a characteristic precipitation and vorticity variability period of about four days.

Following Wheeler and Kiladis (1999), a Fourier-based spatial filter is applied to the daily vorticity field to isolate the large-scale component associated with the TPVSL. The filter retains zonal wavelengths longer than 14° and meridional wavelengths longer than 7°. These thresholds are slightly smaller than the typical TPVSL spatial scale and have been widely used in previous studies of vortex street identification (Liu et al. 2023, 2025).

Following Liu et al. (2025), TPVSL events are identified based on the following principles: (1) Persistent shedding and eastward propagation; any intermittent periods are noted. (2) The interval between shedding events is predominantly 4–5 days. (3) Spatially, small-scale fluctuations are filtered out, retaining only components consistent with the period and spatial scale of the TPVSL. Under these conditions, the identification of the TPVSL is considered successful if the vortex activity maintains a 4–5-day periodic shedding and eastward propagation over time. (4) Additionally, the spatial pattern must exhibit strong similarity to a vortex street configuration: cyclonic activity (e.g., Southwest Vortex, Dabie Vortex) on the southern flank and localized anticyclonic activity (e.g., Lanzhou Small High) on the northern flank.

In this study, six metrics are used to characterize TPVSL activity:

(1) Intensity, defined as the mean positive vorticity within the study region described in Sect. 2.1. Only cyclonic vortices are considered because of their stronger relationship with precipitation.
(2) Shedding period, defined as the mean interval between successive vortex shedding events. Shedding events are identified when the westernmost vortex first appears near 105°E.
(3) Meridional displacement, defined as the change in the mean TPVSL latitude between 1 to 15 May and 16 to 31 May, averaged over 105° to 140°E. The location of the propagation path is shown in Fig. 1b, representing the connecting line between the centers of positive vortices. The average latitude of this line defines the TPVSL propagation path, which exhibits north–south movement.
(4) Zonal propagation speed, defined as the mean eastward propagation speed of the westernmost vortex within 105° to 140°E. The location of maximum vorticity is used as a proxy for the vortex position.
(5) Meridional position, defined as the mean latitude of the TPVSL propagation path averaged over 105° to 140°E during May.
(6) Strouhal number, defined as $St = D / (Te \times U)$, where D is the effective diameter of the Tibetan Plateau (approximately 1000 km), Te is the vortex shedding period, and U is the upstream flow speed. For classical vortex streets, St typically approaches approximately 0.2.

Figure 1 illustrates a typical TPVSL case and the separation of TPVSL-related and unrelated vorticity components. In this study, the position of a TPVSL vortex is defined as the

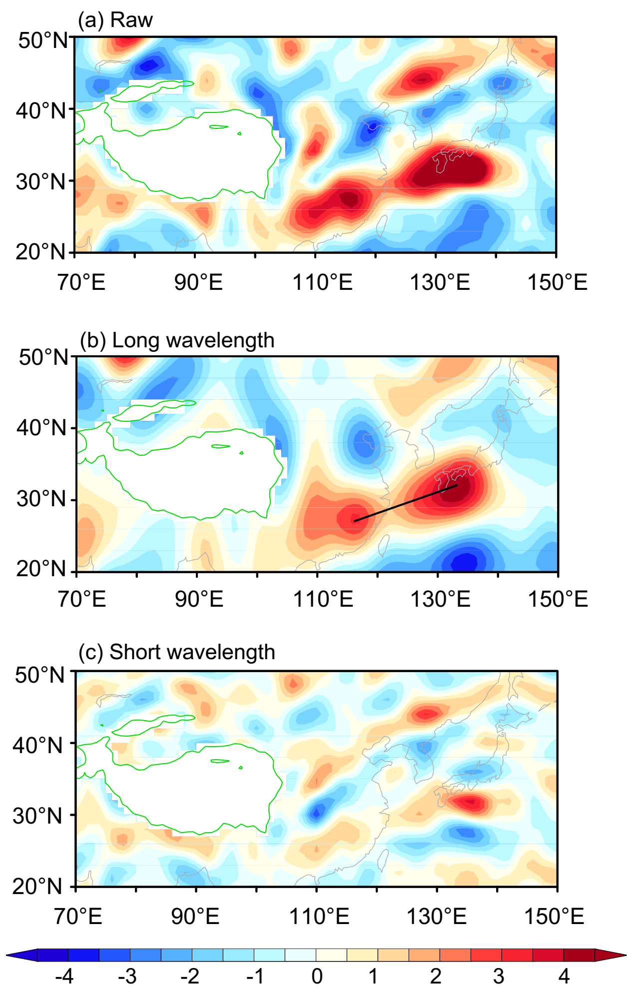

Fig. 1 Example of the TPVSL identification procedure. **a** Raw 700-hPa relative vorticity field. **b** TPVSL-related component obtained by applying a spatial Fourier filter that retains zonal wavelengths longer than 14° and meridional wavelengths longer than 7°. The black line denotes the location of the propagation path. **c** TPVSL-unrelated component containing the remaining smaller-scale variability

location of its maximum vorticity value, the position of the TPVSL propagation path is defined as the connecting line between the maxima of two adjacent vortices, and the intensity of the TPVSL is defined as the mean positive vorticity within the quadrilateral region containing these vortices.

1.3 Identification of precipitation associated with cyclonic activity

To quantify the rainfall linked to cyclonic activity within the TPVSL, we calculate the proportion of precipitation occurring under favorable vortex-induced conditions. Following Hanley and Caballero (2012), regions of cyclonic activity are defined where the filtered relative vorticity is greater than zero. Precipitation associated with the TPVSL is then defined as rainfall falling within these cyclonic regions. The same procedure is applied to both CHIRPS satellite data and CPC ground observations to ensure consistency and comparability. Our focus on precipitation occurring within the cyclonic activity of the TPVSL is because these areas, directly associated with positive vorticity centers (cyclonic circulation), are typically where upward motion and precipitation are strongest.

1.4 Classification of strong and weak TPVSL regimes

TPVSL activity was classified according to the magnitude of the normalized TPVSL strength index. Years with an index greater than + 1 standard deviation were defined as strong TPVSL years, whereas years with an index lower than − 1 standard deviation were defined as weak TPVSL years. Based on this criterion, strong TPVSL years include 1982, 1984, 1987, 1993, 1999, 2004, 2013, 2016, 2021 and 2024, while weak TPVSL years include 1986, 1994, 1995, 2000, 2007, 2008, 2009 and 2012.

2 Results

2.1 Precipitation anomalies associated with strong and weak TPVSL regimes

Based on the TPVSL strength index exceeding one standard deviation above or below the climatological mean, we identify strong TPVSL years and weak TPVSL years during 1979–2025 (Fig. 2a). Figure 2a also shows that May precipitation anomalies over eastern China are strongly correlated with the TPVSL strength index ($r = 0.62$), indicating a close link between vortex street variability and regional rainfall. Composite analyses are then used to compare precipitation anomalies under different TPVSL regimes.

The spatial distributions of May precipitation anomalies during strong and weak TPVSL years are shown in Fig. 2b, c. During strong TPVSL years, eastern China exhibits pronounced wet anomalies, with the largest increases occurring south of the Yangtze River, where mean anomalies reach approximately 100–150 mm. A coherent rainband associated with the TPVSL extends from southwestern China toward the Korea–Japan region. By contrast, weak TPVSL years are characterized by widespread dry anomalies across eastern China and downstream East Asia.

Further analysis of the TPVSL contribution to total precipitation (Fig. 2d, e) indicates that TPVSL-related cyclonic activity accounts for more than 80% of the total May rainfall across most of eastern China, exceeding 90% in parts of the Yangtze River basin during strong TPVSL years. This strong correspondence between TPVSL intensity and

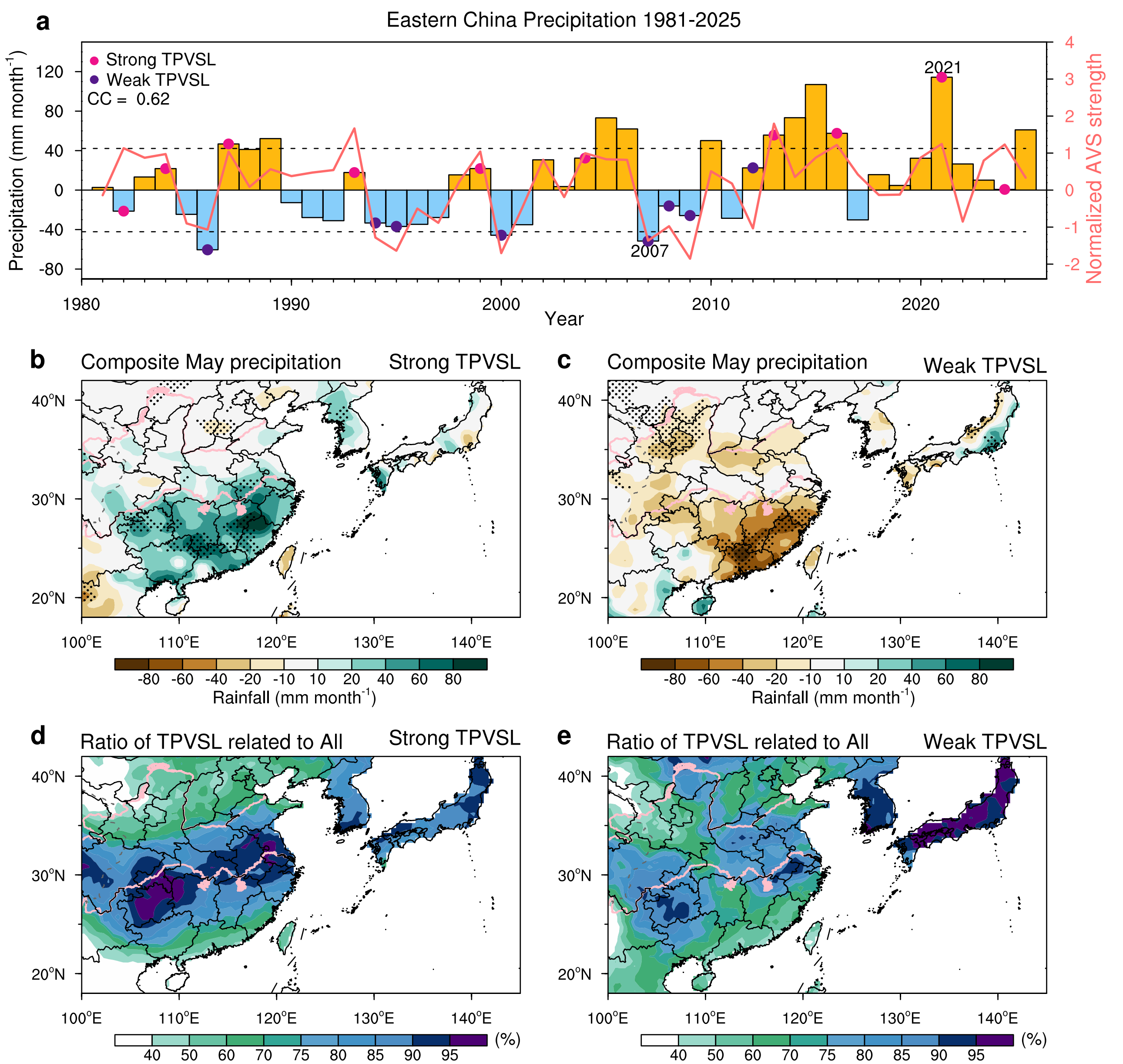

Fig. 2 Eastern China May precipitation anomalies and their relationship with TPVSL strength. **a** Time series of May precipitation anomalies over Eastern China (bars) and the normalized TPVSL strength index (red line) during 1981–2025, derived from the CPC daily precipitation dataset. Precipitation anomalies are calculated relative to the 1981–2010 May climatology. Dashed lines denote ± 1 standard deviation (41.5 mm) of interannual variability. Years with TPVSL strength exceeding + 1 s.d. are defined as strong TPVSL years (pink dots), whereas years with TPVSL strength below − 1 s.d. are defined as weak TPVSL years (purple dots). The Pearson correlation coefficient between the TPVSL index and Eastern China May precipitation anomalies is 0.62. **b**–**c** Composite May precipitation anomalies for strong TPVSL years (**b**) and weak TPVSL years (**c**). Black dots indicate regions where anomalies are significant at the 95% confidence level based on a two-tailed Student's *t* test. **d**–**e** Fraction of total May precipitation (%) associated with TPVSL-related cyclonic activity for strong TPVSL years **d** and weak TPVSL years **e**. The Yangtze River and the Yellow River are shown by pink lines

precipitation anomalies suggests that variations in TPVSL strength play an important role in regulating May rainfall over eastern China.

The climatological distribution of May precipitation over East Asia during 1981–2010 is shown in Fig. 3a. A pronounced rainfall center appears over eastern and southern China, where monthly precipitation exceeds 250 mm in some regions.

Against this climatological background, two representative cases are selected to illustrate TPVSL-related precipitation variability: May 2021, which exhibits the largest precipitation anomaly among strong TPVSL years, and May 2007, one of the driest years associated with exceptionally

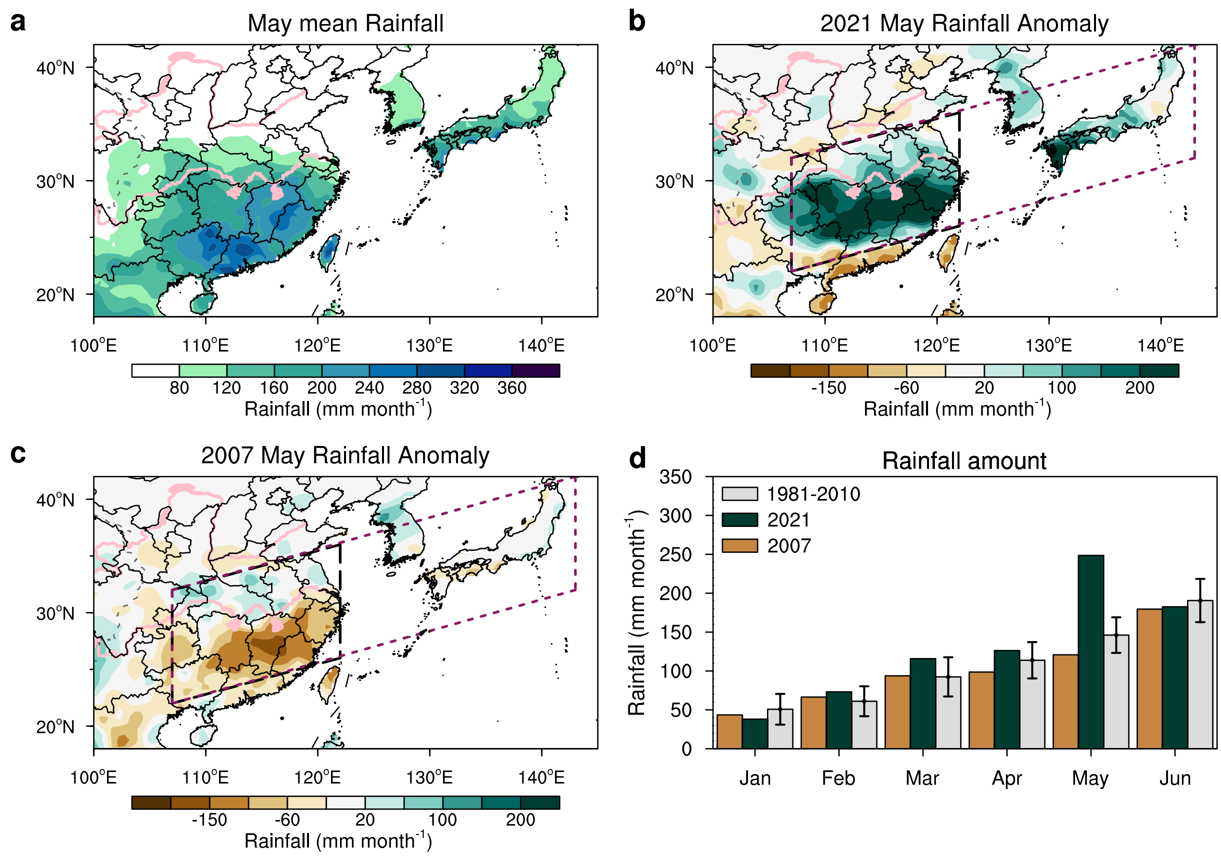

Fig. 3 Spatial distribution and regional characteristics of May precipitation. **a** Climatological mean May precipitation for 1981–2010 (mm month^{-1}). **b**–**c** May precipitation anomalies in 2021 (**b**) and 2007 (**c**). The purple polygon denotes the analysis domain covering Eastern China and the Korea–Japan region. The black dashed polygon indicates Eastern China, and the remaining area represents the Korea–Japan region. Pink lines denote the Yangtze and Yellow Rivers. **d** Monthly precipitation over the combined domain (mm month^{-1}). Bars show values for the 1981–2010 climatology (grey), 2021 (dark green), and 2007 (brown). Error bars indicate ± 1 standard deviation. Precipitation data are derived from the CHIRPS-2.0 satellite–gauge blended dataset

weak TPVSL intensity. In May 2021, precipitation anomalies are strongly positive across southern and eastern China, with a rainband extending northeastward toward Japan (Fig. 3b). In some areas of eastern China and southern Japan, anomalies exceed 150–200 mm month^{-1}. In contrast, May 2007 exhibits widespread negative precipitation anomalies extending from southern China to Japan, with deficits reaching − 150 to − 200 mm month^{-1} in parts of eastern China and Japan (Fig. 3c).

The regional-mean monthly precipitation further highlights the contrast between these two events (Fig. 3d). The climatological May mean precipitation over East Asia is approximately 146 mm month^{-1}, whereas the regional averages reach 249 mm in 2021 and 121 mm in 2007, representing pronounced positive and negative anomalies, respectively. Relative to the interannual standard deviation of May precipitation during 1981–2010 (22 mm), the 2021 event exceeds the climatological mean by roughly four standard deviations, whereas the 2007 event is about one standard deviation below the mean.

2.2 Anomalous vortex street activity modulated the two extreme precipitation events

Figures 4a and 5a show the fraction of total May precipitation explained by the TPVSL in 2021 and 2007. During both events, TPVSL-related rainfall accounted for more than 80% of the total precipitation across the analysis domain. In May 2021, the contribution exhibited a belt-shaped structure extending from Guizhou and Chongqing to Japan and Korea, with values exceeding 95% in the core areas. In contrast, during May 2007 the regions with the largest TPVSL contribution are concentrated over Guizhou, Guangxi and Hunan, as well as parts of Japan and Korea. Moreover, the contribution patterns closely resemble those obtained from the composite analysis (Fig. 2d,e and Figs. 4a and 5a).

To verify that the filtered precipitation represents TPVSL-related rainfall, we examine the corresponding vorticity structures. The filtered vorticity fields display a structure closely resembling an idealized Kármán vortex street, characterized by alternating cyclonic and anticyclonic vortices

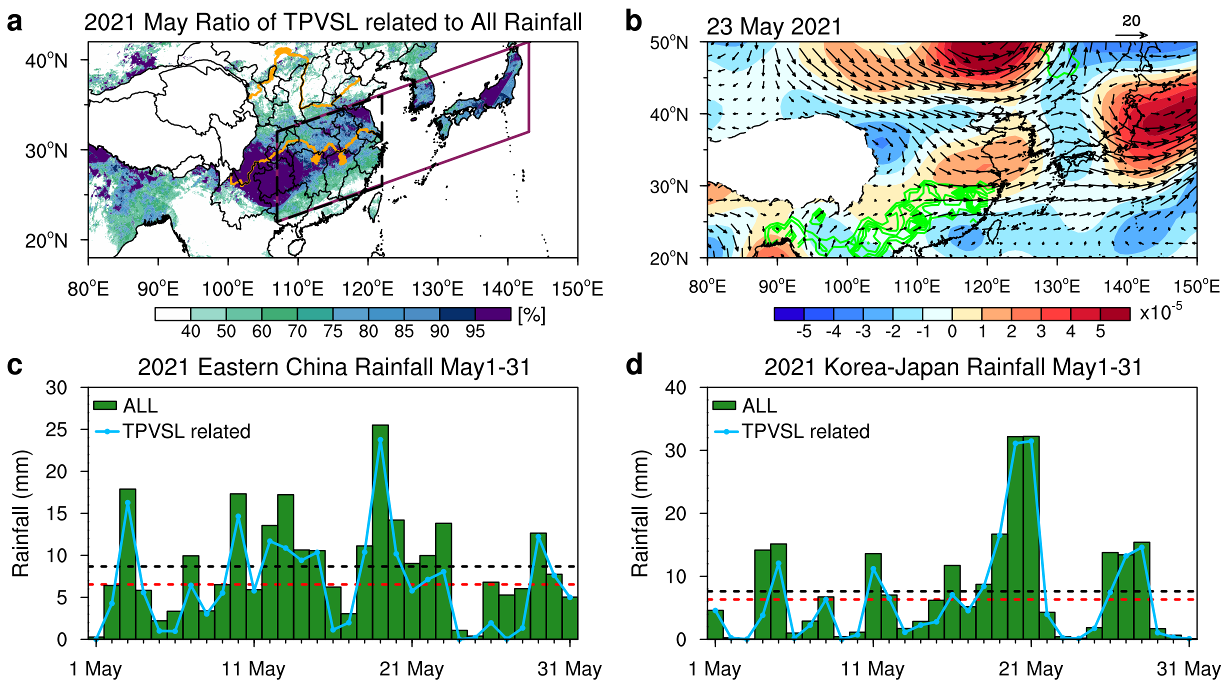

Fig. 4 Contribution of TPVSL to May 2021 precipitation. **a** Fraction of total May precipitation (%) associated with TPVSL cyclonic activity in 2021. The purple polygon outlines the analysis domain spanning the Eastern China and the Korea–Japan region. The black dashed polygon within this domain marks the Eastern China, and the remaining area represents the Korea–Japan region. The orange lines indicate the Yangtze River and the Yellow River. **b** Low-pass filtered horizontal structure of daily relative vorticity (shading; 10^{-5} s^{-1}) and horizontal winds (vectors; m s^{-1}) at 700 hPa on 23 May 2021. Green contours denote daily precipitation (interval = 10 mm), and the dotted black line shows the topographic boundary of the Tibetan Plateau. **c**–**d** Daily total precipitation (green bars) and TPVSL-related precipitation (blue line) averaged over the Eastern China (**c**) and the Korea–Japan region (**d**) during May 2021. Black and red dashed lines indicate the May mean of total and TPVSL-related precipitation, respectively. Precipitation data are taken from the CHIRPS-2.0 satellite–gauge blended data

generated downstream of a topographic obstacle. The patterns in Figs. 4b and 5b closely match the canonical schematic of a vortex street, and their morphology is consistent with fluid dynamics experiments at Reynolds numbers on the order of 10^4 (Khan et al. 2017; Son et al. 2020; Anwar et al. 2022).

The temporal evolution of TPVSL-related precipitation further highlights its important role in regional rainfall (Figs. 4c–d and 5c–d). Over eastern China in May 2021, TPVSL-related precipitation averages 6.5 mm day^{-1} compared with a total rainfall of 8.7 mm day^{-1}. Over the Korea–Japan region, TPVSL-related rainfall averages 6.3 mm day^{-1} while total precipitation reaches 7.6 mm day^{-1}. During May 2007, TPVSL-related precipitation averages 3.9 mm day^{-1} over eastern China and 4.1 mm day^{-1} over the Korea–Japan region, compared with total precipitation amounts of 5.0 and 4.8 mm day^{-1}, respectively.

A prominent feature of both events is the strong synoptic-scale variability, with rainfall events recurring approximately every 3–5 days. This periodic behavior is particularly evident during the 2021 event. Such variability is consistent with previous studies reporting a roughly 4-day precipitation cycle over eastern China (Liu et al. 2008, 2014), suggesting modulation by TPVSL activity. Band-pass filtering within the 3–6 day range further supports this interpretation. The filtered precipitation shows correlations of 0.64 over the Korea–Japan region and 0.77 over eastern China in 2021, indicating that synoptic-scale variability explains a substantial fraction of rainfall variance. Similar behavior is also evident during the 2007 event.

To further characterize the temporal structure of this coupling, Fig. 6 illustrates the longitude–time evolution of TPVSL activity and precipitation. The pronounced periodicity in precipitation is mirrored in the spatiotemporal structure of the vortex street. Vortices are generated with a dominant period of approximately 4–5 days and propagate eastward at a steady speed, closely resembling Kármán vortex street patterns reproduced in laboratory experiments. Precipitation over eastern China also exhibits a similar 4–5-day periodicity and eastward propagation, consistent with the TPVSL signal. The ~4–5-day periodicity is consistent with earlier reports of ~4-day rainfall periodicity over eastern China (Liu et al. 2008, 2014).

The observed periodicity can be interpreted using classical vortex street theory. The Strouhal number, a key dimensionless parameter describing vortex shedding, is approximately 0.2 for Reynolds numbers around 10^4 (Chopra and Hubert 1965; Thomson et al. 1977). Assuming an

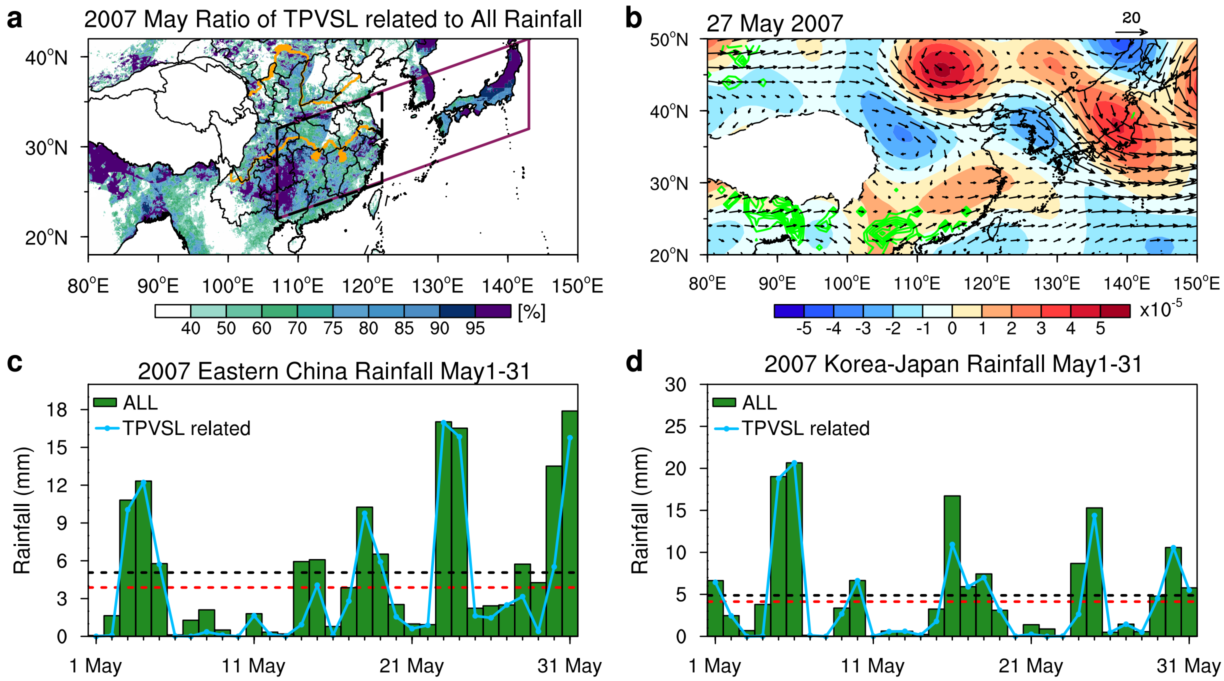

Fig. 5 Contribution of TPVSL to May 2007 precipitation. **a** Fraction of total May precipitation (%) associated with TPVSL cyclonic activity in 2007. The purple polygon outlines the analysis domain spanning the Eastern China and the Korea–Japan region. The black dashed polygon within this domain marks the Eastern China, and the remaining area represents the Korea–Japan region. The orange lines indicate the Yangtze River and the Yellow River. **b** Low-pass filtered horizontal structure of daily relative vorticity (shading; 10^{-5} s^{-1}) and horizontal winds (vectors; m s^{-61}) at 700 hPa on 27 May 2007. Green contours denote daily precipitation (interval = 10 mm), and the dotted black line shows the topographic boundary of the Tibetan Plateau. **c**–**d** Daily total precipitation (green bars) and TPVSL-related precipitation (blue line) averaged over the Eastern China (**c**) and the Korea–Japan region (**d**) during May 2007. Black and red dashed lines indicate the May mean of total and TPVSL-related precipitation, respectively. Precipitation data are taken from the CHIRPS-2.0 satellite–gauge blended data

effective obstacle diameter corresponding to the Tibetan Plateau of about 1000 km and a mean 700 hPa wind speed of 10–15 m s^{-1}, the theoretical shedding period is approximately 4–5 days, which closely matches the observed values. These results support the interpretation that the system maintains a coherent TPVSL structure, providing a favorable dynamical environment for heavy rainfall.

2.3 Long-term TPVSL–rainfall relationship and dynamical characteristics

The influence of TPVSL on May precipitation over East Asia is also evident also evident in the long-term record from 1981 to 2025. Figure 7 shows scatterplots of TPVSL intensity against May precipitation based on CHIRPS-2.0 satellite–gauge estimates and CPC gauge-based precipitation data, for both the Eastern China and the Korea–Japan region. Correlation coefficients range from 0.31 to 0.62 and are statistically significant at the 95% level. Importantly, the strength of the relationship differs by region and dataset. Over eastern China, CPC data yield stronger correlations (r = 0.62) than CHIRPS (r = 0.50). In contrast, over the Korea–Japan region, CHIRPS captures a stronger association (r = 0.42) than CPC (r = 0.31). These differences likely reflect the role of local orography and land–sea contrasts, which exert a greater control on rainfall variability in Korea and Japan (Lee et al. 2014; Kim et al. 2021; Suh et al. 2024). Overall, the results suggest that the detectability of TPVSL impacts on precipitation exhibits strong regional and dataset dependence.

We further examine several dynamical characteristics of the TPVSL under different TPVSL regimes (Fig. 8). The average shedding period is 4.56 days in strong TPVSL years and 4.88 days in weak TPVSL years, both close to the climatological value of 4.65 days. The average vortex propagation speed also varies little among the three categories, with values of 9.33 m s^{-1} in strong TPVSL years, 9.27 m s^{-1} in weak TPVSL years, and 9.14 m s^{-1} in the climatology. Likewise, the mean latitude of the TPVSL propagation line remains close to the climatological position, at 29.98°N in strong TPVSL years and 30.80°N in weak TPVSL years, compared with a climatological mean of 30.49°N. The differences in Te, Ue and Ly between strong and weak TPVSL years are small and fall within the range of interannual variability (Fig. 8).

By contrast, vortex intensity exhibits the clearest separation between the two TPVSL regimes. Strong TPVSL years are characterized by enhanced intensity, with Qe increasing

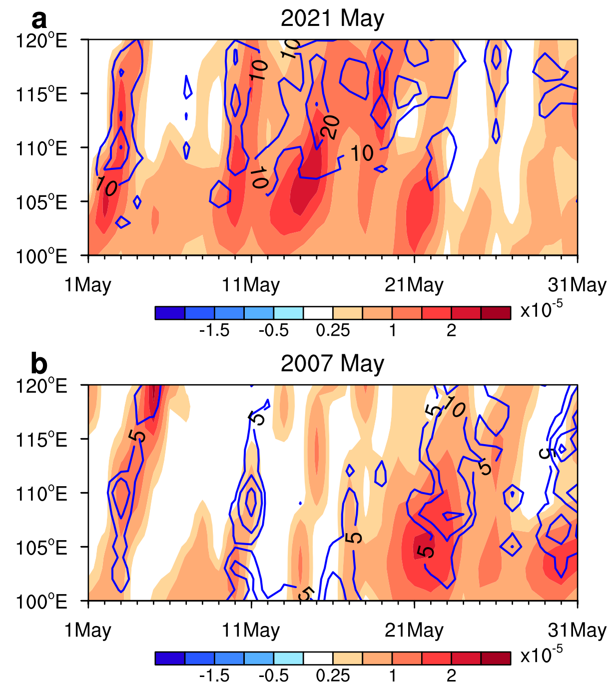

Fig. 6 Evolution of TPVSL and precipitation during May 2021 and 2007. **a** Longitude–time Hovmöller diagram of daily relative vorticity at 700 hPa (shading; $\times 10^{-5}$ s^{-1}), spatially low-pass filtered and averaged over 26–35°N, for May 2021. Blue contours denote daily precipitation averaged over the same latitude band with contour levels of 10, 20, and 30 mm day^{-1}. **b** Same as in (**a**), but for May 2007. Blue contours denote daily precipitation with contour levels of 5, 10, 20, and 30 mm day^{-1}

to approximately 9×10^{-6} s^{-1}, whereas weak TPVSL years show reduced intensity of approximately 5×10^{-6} s^{-1} relative to the climatological mean of about 7×10^{-6} s^{-1}. This contrast indicates that the primary dynamical distinction between strong and weak TPVSL years lies in vortex intensity rather than in propagation speed, shedding period, or mean position. These opposing intensity anomalies provide a dynamical explanation for the contrasting rainfall anomalies associated with the two TPVSL regimes.

Beyond the contrast between strong and weak TPVSL years, the TPVSL also exhibits clear seasonal evolution from late spring to early summer. In May, the mean propagation speed is about 9 m s^{-1} (Fig. 8b). Previous studies have shown that this speed decreases to roughly 6 m s^{-1} during June–July (Liu et al. 2025), consistent with the seasonal weakening of the background westerlies. At the same time, whereas the TPVSL propagation latitude remains nearly stationary in May, the system undergoes a pronounced northward shift during June–July following the rapid northward migration of the westerly jet (Liu et al. 2023, 2025). This behavior is consistent with fluid dynamical theory, in which the downstream propagation speed of a vortex street is closely linked to the upstream flow velocity (Wu 1999; Liu et al. 2023). These seasonal contrasts further highlight the dynamical linkage between TPVSL activity and the large-scale circulation background.

2.4 Anomalous circulation modulates the vortex street structure

Previous studies have shown that TPVSL variability during June–July is strongly influenced by large-scale circulation features, including upstream and downstream westerlies, the Western Pacific Subtropical High, and the Tibetan Plateau itself (Liu et al. 2019, 2023, 2025; Li et al. 2021). An important question is whether the May TPVSL anomalies during heavy precipitation years are similarly modulated by the surrounding circulation.

The intensity of the May TPVSL is closely linked to anomalous westerlies upstream of the Plateau and along the southern branch of the flow around it. Earlier studies suggested that vortex street intensity is regulated by the strength of the upstream inflow together with airflow bypassing the northern and southern flanks of the Plateau (Zhang and Guo 2005; Ding et al. 2021), consistent with classical Kármán vortex street dynamics derived from fluid mechanics (Bearman 1967; Mowlavi et al. 2016) and supported by numerical simulations (Liu et al. 2025).

Following Liu et al. (2025), we examine the relationship between the 700 hPa westerly jet and TPVSL intensity. The correlation pattern (Fig. 9a) reveals a pronounced positive center south of the Tibetan Plateau, collocated with the southern branch of the flow around the Plateau. Accordingly, the 700 hPa zonal wind averaged over 95–105°E and 15–25°N is used to define the upstream wind index representing the strength of the incoming flow. This region corresponds to the southern branch of the upstream westerly flow approaching the southeastern flank of the Tibetan Plateau.

The scatterplot in Fig. 9b shows a significant positive relationship between the upstream 700 hPa zonal wind index and TPVSL intensity. Most strong TPVSL years fall in the upper-right quadrant of the scatterplot (9 out of 10), whereas most weak TPVSL years lie in the lower-left quadrant (6 out of 8). The mean upstream wind speed is approximately 5.7 m s^{-1} in strong TPVSL years and 3.6 m s^{-1} in weak TPVSL years. Overall, the TPVSL intensity index is significantly correlated with the upstream zonal wind index ($r = 0.64$, $p < 0.001$), indicating that strengthened southern-branch westerlies favor TPVSL intensification, while weakened upstream flow corresponds to reduced vortex activity.

It is worth noting that strong correlations are mainly distributed on the northern and southern sides of the Plateau. This study focuses on the northern and southern Tibetan Plateau because the westerly winds in these regions exhibit the strongest and most stable temporal correlation with TPVSL intensity, likely reflecting the intensity of upstream westerly

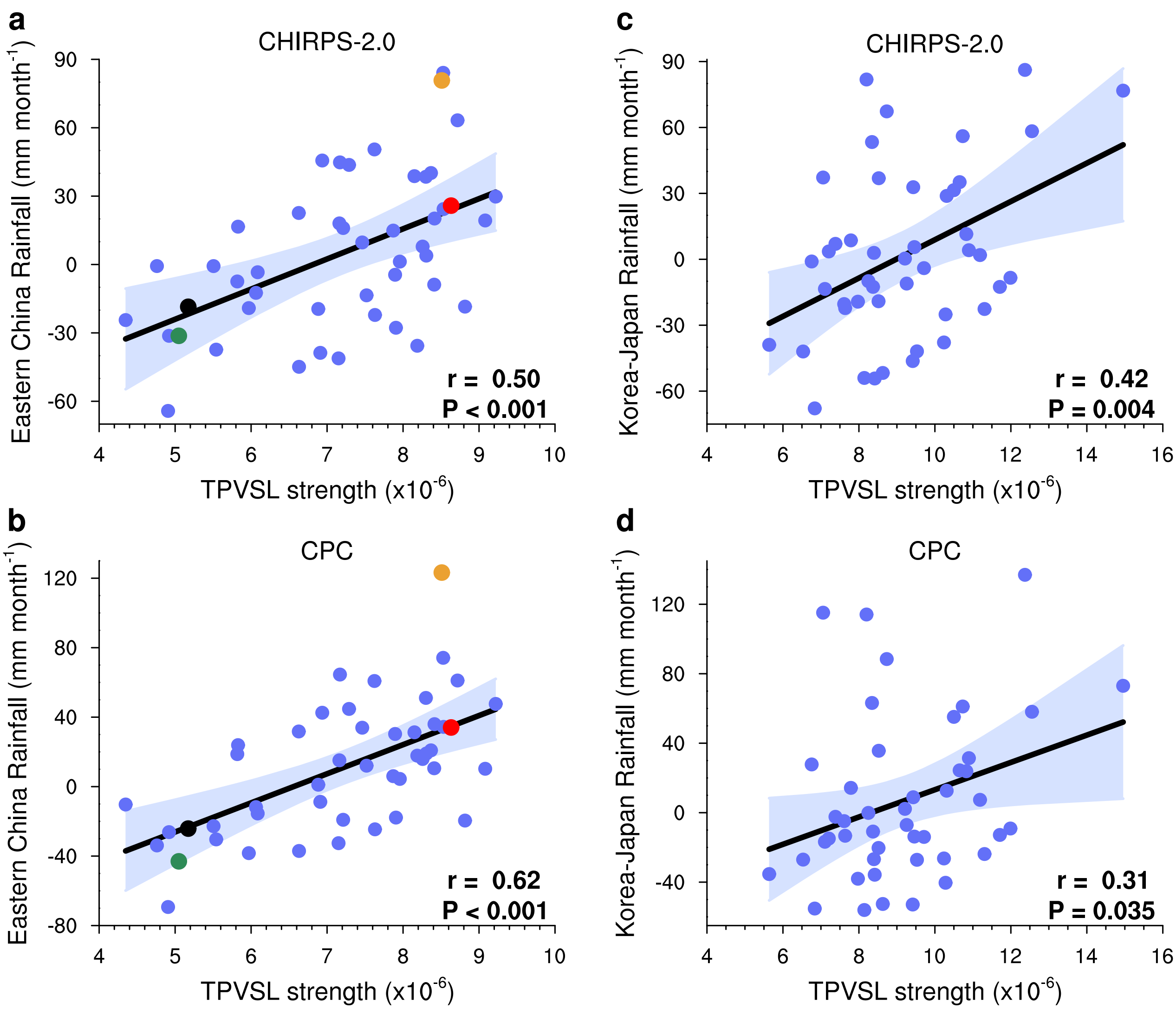

Fig.7 Relationship between TPVSL intensity and May rainfall over Eastern China and the Korea–Japan region using CHIRPS-2.0 and CPC datasets. **a**–**b** Relationship between regional mean May rainfall (y-axis; mm month^{-1}) and TPVSL intensity (x-axis; $\times 10^{-6}$ s^{-1}) during 1981–2025 for Eastern China based on CHIRPS-2.0 precipitation data (**a**) and CPC daily precipitation data (**b**). Solid lines denote least-squares fits and shaded bands indicate 95% confidence intervals. Pearson correlation coefficients (r) with corresponding significance levels (P) are shown. The red and black dots denote the mean states for strong and weak TPVSL years, respectively. May 2021 and May 2007 are highlighted by orange and green circles, respectively. **c**–**d** Same as (**a**–**b**), but for the Korea–Japan region

jet branches and flow around the plateau, which have a direct dynamic effect on vortex generation and downstream transport. The strong negative correlation over the Indian Ocean may be more associated with Indian monsoon or southern branch trough activity, and its physical link to the TPVSL may be more indirect.

The stability of TPVSL position in May is also closely related to the downstream westerly jet. Previous studies have shown that the downstream jet influences both the position of the East Asian rainband (Zhang and Guo 2005; Liu et al. 2019) and the TPVSL itself (Liu et al. 2023, 2025). The intraseasonal displacement of the summer TPVSL has likewise been linked to variations in the downstream jet (Chiang et al. 2020; Kong and Chiang 2020). Extending this framework, we examine whether intramonthly jet variations in May influence TPVSL position. The latitudinal shifts of the 200 hPa westerly jet are significantly positively correlated with changes in the TPVSL propagation line over 110°–130°E (Fig. 10; r=0.52, p<0.001). This behavior is consistent with fluid dynamical theory, in which downstream westerlies provide the background flow guiding vortex propagation (Wang and Alben 2015). Meanwhile, no substantial difference is found in the mean propagation latitude between strong and weak TPVSL years, confirming exceptional stability. This stability provided a favorable dynamical background for the persistence positioning of the

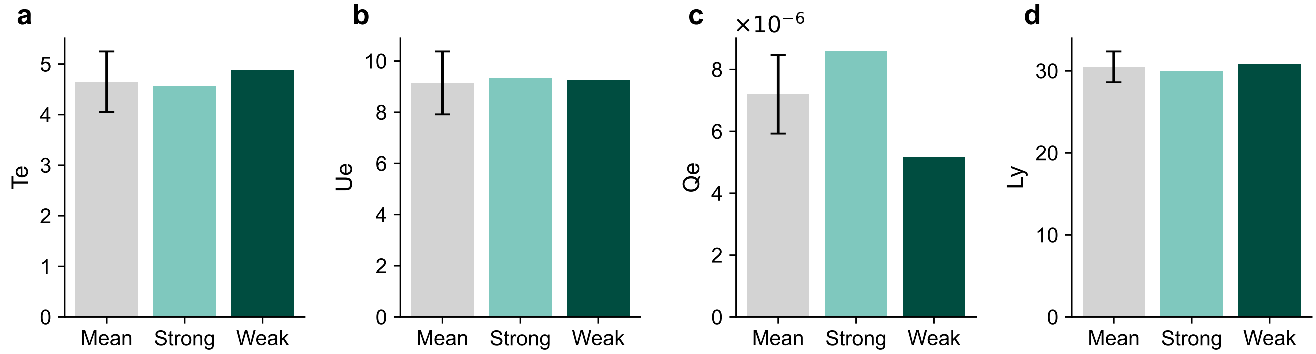

Fig. 8 Variations in TPVSL metrics under different TPVSL regimes. **a**–**d** Comparison of the climatological May mean (grey), strong TPVSL years (light green), and weak TPVSL years (dark green) for (**a**) the average shedding period (Te, days), **b** the average vortex propagation speed (Ue, m s^{-1}), **c** the average vortex intensity (Qe, $\times 10^{-6}$ s^{-1}), and **d** the mean latitudinal position of the TPVSL propagation path (Ly, °N). Error bars indicate ± 1 standard deviation of interannual variability during 1981–2025

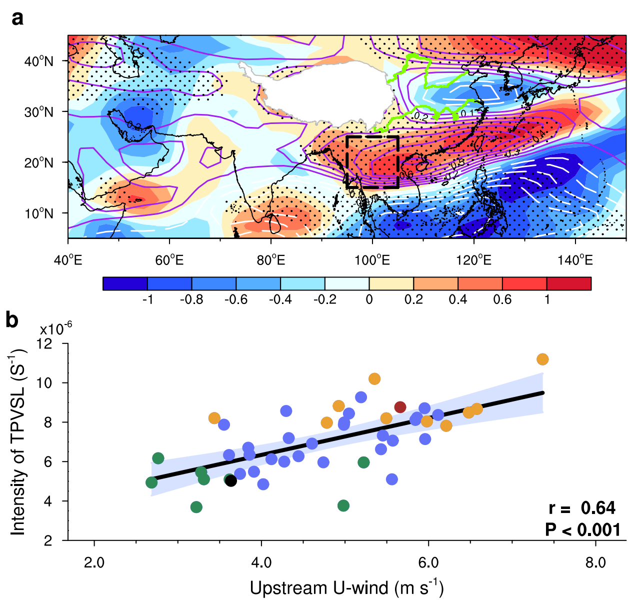

Fig. 9 Impact of upstream westerlies on TPVSL intensity. **a** Spatial distribution of mean 700 hPa zonal wind anomalies (shading; m s^{-1}) when the 200 hPa westerly jet over 80–100°E is located near 31°N. Purple and white contours denote positive and negative correlations, respectively, between upstream 700 hPa zonal wind and mean TPVSL intensity (interval = 0.1). Black dots indicate statistical significance at the 95% confidence level. The black box marks the upstream region (95–105°E, 15–25°N) used to define the zonal wind index. **b** Relationship between the upstream 700 hPa zonal wind averaged over 95–105°E, 15–25°N and the mean TPVSL intensity at 700 hPa (10^{-6} s^{-1}) during 1981–2025. Orange and green dots denote strong and weak TPVSL years, respectively, while blue dots represent the remaining years. The red and black dots denote the mean states for strong and weak TPVSL years, respectively. The correlation coefficient (r) and significance level (P) are shown

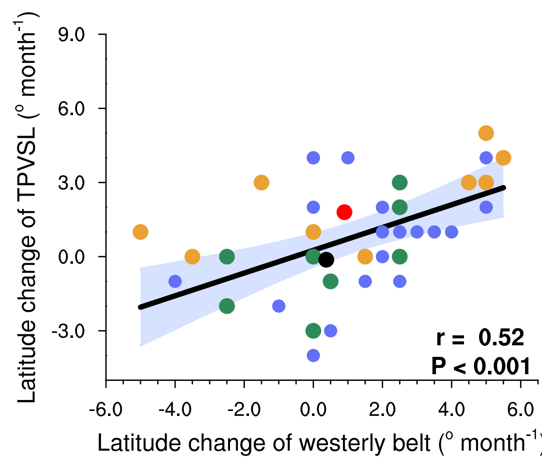

Fig. 10 Relationship between changes in the latitude of the 200 hPa westerly jet over 110–130°E and changes in the latitudinal position of the TPVSL propagation line in May during 1981–2025. Orange and green dots denote strong and weak TPVSL years, respectively, while blue dots represent the remaining years. The red and black dots denote the mean states for strong and weak TPVSL years, respectively. The correlation coefficient (r) and significance level (P) are shown

TPVSL and the associated rainband over southern China, the Korean Peninsula, and Japan.

These results indicate that extreme May precipitation events are associated with distinct vortex street states. In strong TPVSL years, enhanced upstream westerlies intensify the vortex street, while the downstream jet helps anchor its position. In weak TPVSL years, weakened upstream westerlies correspond to reduced vortex activity, although the downstream jet continues to constrain the propagation latitude. Together, these circulation anomalies regulate TPVSL intensity and position, allowing the vortex street to exert a sustained influence on East Asian precipitation.

2.5 Moisture transport and vertical motion associated with TPVSL anomalies

As previously mentioned, the TPVSL only provides a favorable background condition for May precipitation in East Asia, while rainfall itself results from the interaction of multiple factors. To further explore this, we analyze the distributions of low-level moisture transport and mid-tropospheric vertical motion during strong and weak TPVSL years.

Composite fields of 850-hPa moisture flux and 500-hPa vertical velocity (Fig. 11) reveal a coherent band of enhanced ascent during strong TPVSL years and in May 2021. This ascending belt extends from southwestern China, including Sichuan and Yunnan, northeastward toward the Korean Peninsula and Japan, broadly following the downstream propagation pathway of the vortex street. Along this corridor, negative ω anomalies dominate, indicating strengthened upward motion associated with the TPVSL. In contrast, weak TPVSL years and May 2007 exhibit suppressed ascent or weak subsidence along the same pathway.

Low-level moisture transport exhibits a similar contrast. During strong TPVSL years and in May 2021 (Fig. 11a, c), enhanced moisture transport occurs along two main pathways. One pathway originates from the South China Sea and the western Pacific, with strengthened southwesterlies advecting moisture northward toward eastern China, Korea, and Japan. A second pathway extends from the tropical Indian Ocean and converges along the East Asian rainband. In weak TPVSL years and in May 2007, both pathways are substantially weakened (Fig. 11b, d).

Compared with neutral TPVSL years, strong TPVSL years exhibit a clear alignment between the ascending motion belt, enhanced moisture transport, and the TPVSL propagation pathway (Fig. 11a). This suggests that intensified vortex street activity enhances ascent and moisture supply along the TPVSL pathway, thereby amplifying regional precipitation anomalies. In contrast, weak TPVSL years are characterized by suppressed ascent and reduced moisture transport along the same pathway, contributing to weaker precipitation (Fig. 11b).

These results indicate that extreme May precipitation events arise from the interaction between TPVSL dynamics and favorable moisture conditions, rather than from TPVSL variability alone. The convergence of multiple favorable conditions significantly amplified the extremity of the heavy rainfall events.

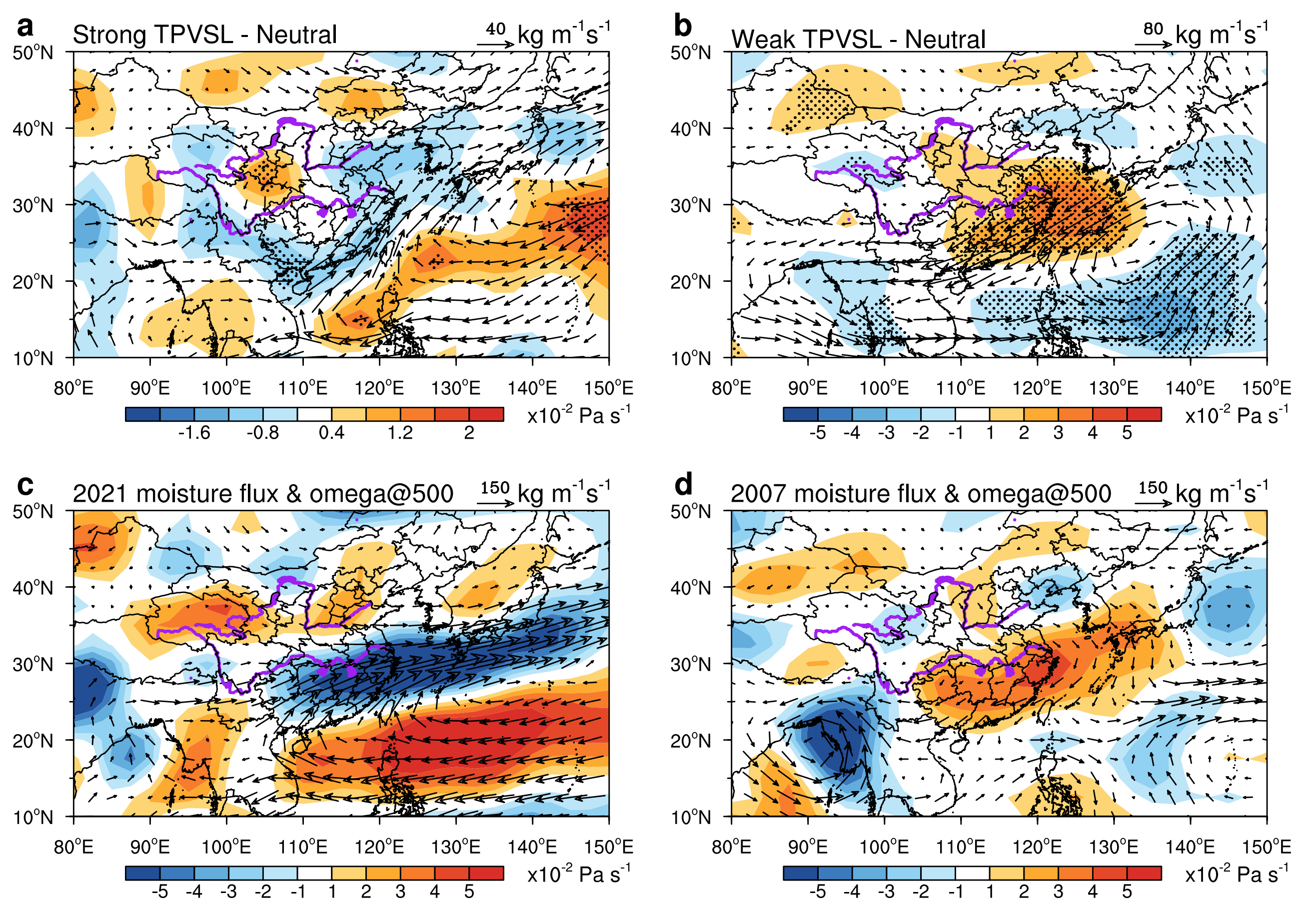

Fig. 11 Moisture transport and vertical motion associated with TPVSL variability. **a** Composite difference in 850-hPa moisture flux (vectors; reference vector 40 kg m^{-1} s^{-1}) and 500-hPa vertical velocity (ω; shading; $\times 10^{-2}$ Pa s^{-1}) for strong TPVSL years minus neutral years. **b** Same as (**a**) but for weak TPVSL years minus neutral years. Dots indicate regions significant at the 95% confidence level. **c**–**d** Monthly mean 850-hPa moisture flux (vectors; reference vector 150 kg m^{-1} s^{-1}) and 500-hPa vertical velocity (ω; shading; $\times 10^{-2}$ Pa s^{-1}) for May 2021 (**c**) and May 2007 (**d**)

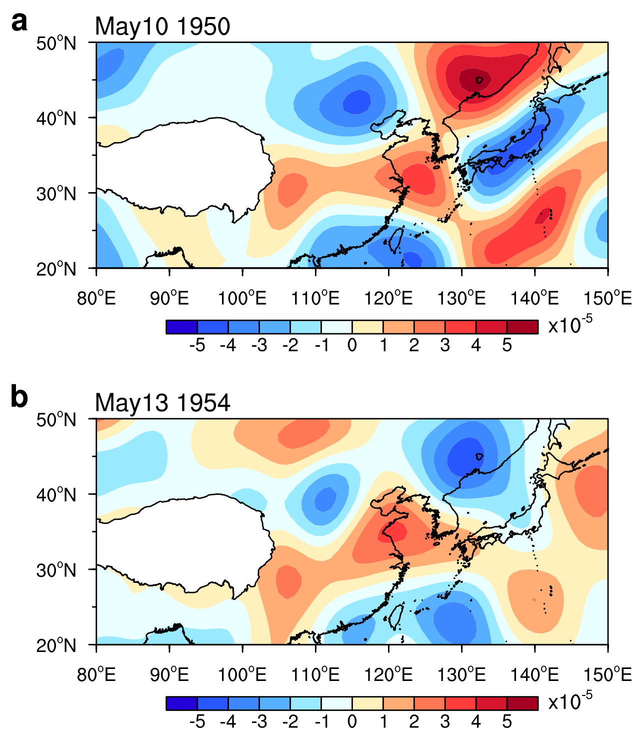

Fig. 12 Examples of TPVSL vortex street structures in the ACCESS-ESM1-5 historical simulation. **a**–**b** Low-pass spatially filtered daily relative vorticity at 700 hPa (shading; $\times 10^{-5}$ s^{-1}) on (**a**) 10 May 1950 and **b** 13 May 1954

2.6 Model evaluation using ACCESS-ESM1—5

To assess whether the observed TPVSL–precipitation relationship is reproduced in climate models, we analyze May vortex street activity and precipitation in the ACCESS-ESM1—5 historical simulation following Liu et al. (2025).

The ACCESS-ESM1—5 simulation reproduces the horizontal structure of daily 700-hPa relative vorticity associated with the TPVSL, as illustrated by two representative cases (Fig. 12). The model captures the key spatial characteristics identified in the reanalysis, including alternating cyclonic and anticyclonic vortices extending eastward from the eastern flank of the Tibetan Plateau. Cyclonic activity initiates near the southeastern flank of the Tibetan Plateau and propagates downstream toward eastern China, the Korean Peninsula, and parts of Japan, consistent with the observed TPVSL structure.

We then examine whether the model reproduces the relationship between TPVSL intensity and precipitation across downstream regions. Scatterplots of TPVSL intensity and regional mean May precipitation show significant positive correlations in both eastern China and the Korea–Japan region (Fig. 13). The correlation coefficient reaches 0.50 in eastern China and 0.42 over Korea–Japan, both exceeding the 99% confidence level. The model also reproduces the stronger TPVSL–precipitation relationship over eastern

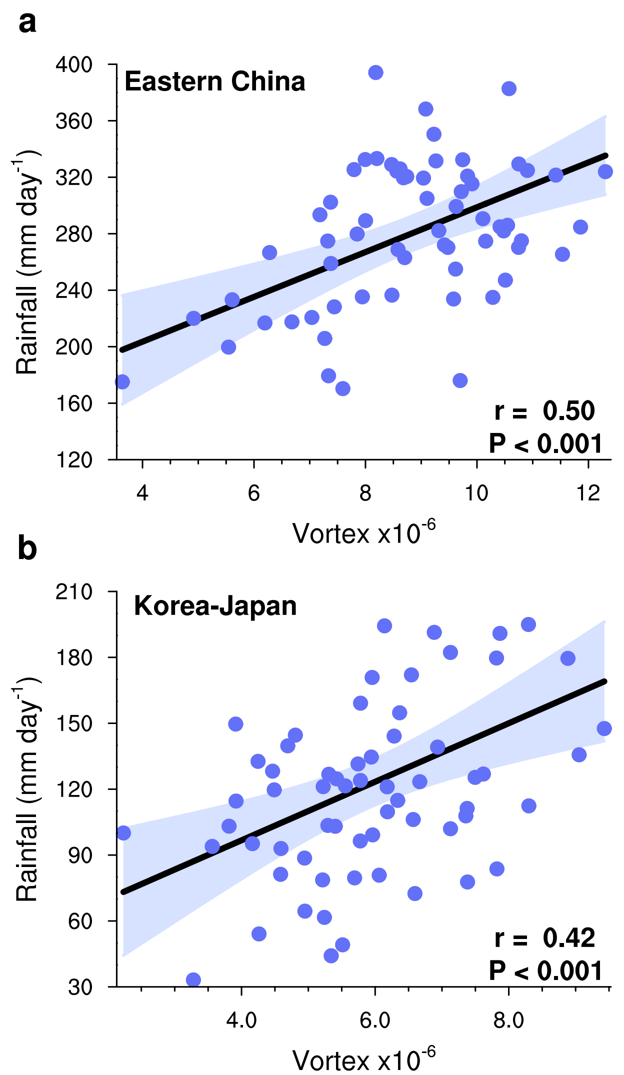

Fig. 13 Relationship between TPVSL intensity and precipitation in the ACCESS-ESM1—5 historical simulation. **a**–**b** Regional mean May precipitation (mm day^{-1}) versus TPVSL intensity ($\times 10^{-6}$ s^{-1}) for (**a**) eastern China and (**b**) the Korea–Japan region. Solid lines indicate least-squares fits and shading denotes the 95% confidence interval. Pearson correlation coefficients (r) and P values are shown

China than over the Korea–Japan region, consistent with the observational analysis (Fig. 7).

The model further captures the observed tendency for strong TPVSL years to coincide with enhanced precipitation over the middle and lower reaches of the Yangtze River Valley. These results provide independent support for the observational results and suggests that this association may have climatic significance.

3 Discussion

This study investigates the role of the Tibetan Plateau vortex street–like (TPVSL) system in regulating May precipitation across East Asia using CHIRPS-2.0 satellite–gauge blended precipitation data, CPC gauge observations, and reanalysis products. Two representative events are examined as typical examples of strong and weak TPVSL regimes: May 2021, characterized by exceptionally strong TPVSL activity, and May 2007, representing a weak TPVSL case. These events exhibit contrasting precipitation anomalies, with the 2021 event featuring an intense rainband extending from southern China to Japan, whereas the 2007 event shows widespread precipitation suppression across eastern China, the Korean Peninsula, and Japan.

Our results indicate that the TPVSL provides the important circulation background for these precipitation events. TPVSL-related cyclonic activity accounts for more than 80% of the total May rainfall across much of eastern China and exceeds 95% in core regions. Despite the contrasting rainfall outcomes, the TPVSL in both cases exhibits a similar dynamical structure with a stable intramonthly propagation position, whereas the primary distinction lies in vortex intensity. These dynamical conditions produce pronounced 3–5-day variability in precipitation associated with TPVSL activity, consistent with the theoretical vortex shedding period inferred from Strouhal number scaling. The influence of TPVSL activity on May precipitation is further supported by the ACCESS-ESM1—5 model simulation, which reproduces both the vortex street structure and its statistical relationship with regional rainfall.

Long-term analysis over 1981–2025 further confirms a significant relationship between TPVSL intensity and May precipitation across East Asia, with correlation coefficients ranging from approximately 0.3 to 0.6. The strength of this relationship varies across regions and datasets. Gauge-based CPC observations capture a stronger TPVSL–precipitation linkage over eastern China, whereas the satellite–gauge blended CHIRPS-2.0 dataset shows higher correlations over the Korea–Japan region. These differences likely reflect variations in observational coverage and regional precipitation characteristics, highlighting the regional and dataset dependence of the TPVSL–precipitation relationship.

Our results also demonstrate that TPVSL variability is closely modulated by the surrounding large-scale circulation. Enhanced upstream westerlies south of the Tibetan Plateau strengthen the vortex street, while the downstream westerly jet helps maintain a stable propagation latitude. The combined influence of these circulation anomalies regulates both the intensity and position of the TPVSL, thereby creating favorable conditions for either enhanced or suppressed rainfall along the downstream rainband.

Theoretical interpretations of vortex streets are typically derived from idealized fluid dynamics models, such as the classical cylinder wake, which assume uniform inflow and negligible vertical shear. Fluid dynamical theory suggests that the flow separation near the obstacle plays the important role in generating vortex shedding, implying that vertical shear may exert a relatively secondary influence on the formation of vortex streets. Indeed, the simple cylinder-wake framework provides a useful explanation for the observed 3–5-day periodicity of vortex activity and precipitation over East Asia. Nevertheless, the real atmosphere exhibits substantial vertical wind shear, which may influence vortex development and propagation. Investigating the role of vertical shear in TPVSL dynamics remains an important topic for future work.

Overall, these findings highlight the TPVSL as an important dynamical mechanism shaping extreme May precipitation across East Asia. The results demonstrate that TPVSL activity remains dynamically influential during late spring, extending its impact beyond the better-known early summer vortex street regime. In the future, we will study the characteristics of classification based on other TPVSL indicators (such as shedding period, vortex speed) and their impact on precipitation. Monitoring TPVSL anomalies could improve the early detection of flood disasters, inform flood control and agricultural management, and support more realistic simulation and prediction of East Asian rainfall in climate models.

Author Contributions Conceptualization, R.G and G.H; methodology, R.G; software, R.G; validation, R.G; formal analysis, R.G; investigation, R.G; resources, R.G; data curation, R.G; writing—original draft preparation, R.G; writing—review and editing, R.G, G.H; visualization, R.G; supervision, G.H; project administration, G.H; funding acquisition, G.H All authors have read and agreed to the published version of the manuscript.

Funding This research was funded by the National Natural Science Foundation of China (Grant Nos. 42530606, 42261144687 and 42406006) and the National Key R&D Program of China (2025YFF0812000).

Data Availability The CHIRPS-2.0 precipitation dataset is available at https://data.chc.ucsb.edu. The CPC precipitation dataset is available at https://psl.noaa.gov/data/gridded/data.cpc.globalprecip.html. The NCEP/NCAR reanalysis dataset is available at https://esrl.noaa.gov/psd/data/gridded/data.ncep.reanalysis.html. The ERA5 reanalysis dataset is at https://doi.org/10.24381/cds.adbb2d47.

Declarations

Competing interest The authors have no relevant financial or non-financial interests to disclose.

References

Anwar MU et al (2022) Effect of variation in the mass ratio on vortex-induced vibration of a circular cylinder in crossflow direction at Reynold number = 10^4: a numerical study using RANS model. J Mar Sci Eng 10:1126

Bearman PW (1967) On vortex street wakes. J Fluid Mech 28:625–641. https://doi.org/10.1017/S0022112067002368

Chen M, Shi W, Xie P, Silva VBS, Kousky VE, Wayne Higgins R, Janowiak JE (2008) Assessing objective techniques for gauge-based analyses of global daily precipitation. J Geophys Res Atmos 5:113. https://doi.org/10.1029/2007JD009132

Chiang JCH, Kong W, Wu CH, Battisti DS (2020) Origins of East Asian summer monsoon seasonality. J Clim 33:7945–7965. https://doi.org/10.1175/JCLI-D-19-0888.1

Chopra KP, Hubert LF (1965) Mesoscale eddies in wake of islands. J Atmos Sci 22:652–657

Curio J, Schiemannm R, Hodges KI, Turner AG (2019) Climatology of Tibetan Plateau vortices in reanalysis data and a high-resolution global climate model. J Clim 32:1933–1950. https://doi.org/10.1175/JCLI-D-18-0021.1

Ding Y (1992) Effects of the Qinghai-Xizang (Tibetan) Plateau on the circulation features over the plateau and its surrounding areas. Adv Atmos Sci 9:112–130. https://doi.org/10.1007/BF02656935

Ding Y, Liu Y, Hu Z-Z (2021) The record-breaking Mei-yu in 2020 and associated atmospheric circulation and tropical SST anomalies. Adv Atmos Sci 38:1980–1993. https://doi.org/10.1007/s00376-021-0361-2

Feng J, Li J (2011) Influence of El Niño Modoki on spring rainfall over south China. J Geophys Res Atmos. https://doi.org/10.1029/2010JD015160

Fu S-M, Li W-L, Ling J (2015) On the evolution of a long-lived mesoscale vortex over the Yangtze River Basin: geometric features and interactions among systems of different scales. J Geophys Res Atmos 120:11889–11917. https://doi.org/10.1002/2015JD023700

Fu S-M, Zhang J-P, Sun J-H, Zhao T-B (2016) Composite analysis of long-lived mesoscale vortices over the middle reaches of the Yangtze River valley: octant features and evolution mechanisms. J Clim 29:761–781. https://doi.org/10.1175/JCLI-D-15-0175.1

Funk C et al (2015) The Climate Hazards Infrared Precipitation with Stations, a new environmental record for monitoring extremes. Sci Data 2:150066. https://doi.org/10.1038/sdata.2015.66

Gu W, Wang L, Hu Z-Z, Hu K, Li Y (2018) Interannual variations of the first rainy season precipitation over South China. J Clim 31:623–640. https://doi.org/10.1175/JCLI-D-17-0284.1

Gu L, Sun J, Yu S, Zhang M (2021) Footprints of Pacific Decadal Oscillation in the interdecadal variation of Consecutive Cloudy-Rainy Events in Southern China. Atmo Res 257:105609. https://doi.org/10.1016/j.atmosres.2021.105609

Han J et al (2024) Threat of low-frequency high-intensity floods to global cropland and crop yields. Nat Sustain 7:994–1006. https://doi.org/10.1038/s41893-024-01375-x

Hanley J, Caballero R (2012) Objective identification and tracking of multicentre cyclones in the ERA-Interim reanalysis dataset. Q J R Meteorol Soc 138:612–625

Hersbach H et al (2020) The ERA5 global reanalysis. Q J R Meteorol Soc 146:1999–2049. https://doi.org/10.1002/qj.3803

Huang G, Zhou L (2004) The variability of the wind system circulating round the west side of the Tibetan Plateau and its relation to the East Asian summer monsoon and summer rainfall in North China. Clim Environ Res 9:317–330

Huang D-Q, Zhu J, Zhang Y-C, Wang J, Kuang X-Y (2015) The impact of the East Asian Subtropical Jet and Polar Front Jet on the frequency of spring persistent rainfall over Southern China in 1997–2011. J Clim 28:6054–6066. https://doi.org/10.1175/JCLI-D-14-00641.1

Jia X, You Y, Wu R, Yang Y (2019) Interdecadal changes in the dominant modes of the interannual variation of spring precipitation over China in the Mid-1980s. J Geophys Res Atmos 124:10676–10695. https://doi.org/10.1029/2019JD030901

Jia X, Zhang C, Wu R, Qian Q (2021) Changes in the relationship between spring precipitation in Southern China and Tropical Pacific-South Indian Ocean SST. J Clim 34:6267–6279. https://doi.org/10.1175/JCLI-D-20-0817.1

Kalnay E et al (1996) The NCEP/NCAR 40-year reanalysis project. Bull Am Meteor Soc 77:437–472

Khan NB, Ibrahim Z, Nguyen LTT, Javed MF, Jameel M (2017) Numerical investigation of the vortex-induced vibration of an elastically mounted circular cylinder at high Reynolds number (Re = 10^4) and low mass ratio using the RANS code. PLoS ONE 12:e0185832. https://doi.org/10.1371/journal.pone.0185832

Kim K, Bang W, Chang EC, Tapiador FJ, Tsai CL, Jung E, Lee G (2021) Impact of wind pattern and complex topography on snow microphysics during International Collaborative Experiment for PyeongChang 2018 Olympic and Paralympic winter games (ICE-POP 2018). Atmos Chem Phys 21:11955–11978. https://doi.org/10.5194/acp-21-11955-2021

Kim Y-U, Webber H, Adiku SG, Júnior RdSN, Deswarte J-C, Asseng S, Ewert F (2024) Mechanisms and modelling approaches for excessive rainfall stress on cereals: waterlogging, submergence, lodging, pests and diseases. Agric for Meteorol 344:109819. https://doi.org/10.1016/j.agrformet.2023.109819

Kong W, Chiang JC (2020) Interaction of the westerlies with the Tibetan Plateau in determining the Mei-yu termination. J Clim 33:339–363

Lee K-OK, Uyeda H, Lee DI (2014) Effect of an isolated elliptical terrain (Jeju Island) on rainfall enhancement in a moist environment. Tellus A Dyn Meteorol Oceanogr 66:20484. https://doi.org/10.3402/tellusa.v66.20484

Li L, Zhu C, Zhang R, Liu B (2021) Roles of the Tibetan Plateau vortices in the record Meiyu rainfall in 2020. Atmos Sci Lett 22:e1017. https://doi.org/10.1002/asl.1017

Liu H, Zhang D-L, Wang B (2008) Daily to submonthly weather and climate characteristics of the summer 1998 extreme rainfall over the Yangtze River Basin. J Geophys Res Atmos. https://doi.org/10.1029/2008JD010072

Liu H-B, Yang J, Zhang D-L, Wang B (2014) Roles of synoptic to quasi-biweekly disturbances in generating the summer 2003 heavy rainfall in East China. Mon Weather Rev 142:886–904. https://doi.org/10.1175/MWR-D-13-00055.1

Liu Q, Zhou T, Mao H, Fu C (2019) Decadal variations in the relationship between the Western Pacific Subtropical High and summer heat waves in East China. J Clim 32:1627–1640. https://doi.org/10.1175/JCLI-D-18-0093.1

Liu Q, Wu Z, Tan Z-M, Yang F, Fu C (2023) The atmospheric vortex streets and their impact on precipitation in the wake of the Tibetan Plateau. Atmosphere 14:1096

Liu Q, Fu C, Xu Z (2025) The key role of abnormal vortex street-like system in the Tibetan Plateau's wake in modulating extreme June-July rainfall events over Eastern China (2020 and 2024). Clim Dyn 63:216. https://doi.org/10.1007/s00382-025-07708-6

Mowlavi S, Arratia C, Gallaire F (2016) Spatio-temporal stability of the Kármán vortex street and the effect of confinement. J Fluid Mech 795:187–209

O'Neill BC, Tebaldi C, Van Vuuren DP et al (2016) The scenario model intercomparison project (ScenarioMIP) for CMIP6. Geosci Model Dev 9(9):3461–3482

Ombadi M, Risser MD, Rhoades AM, Varadharajan C (2023) A warming-induced reduction in snow fraction amplifies rainfall

extremes. Nature 619:305–310. https://doi.org/10.1038/s41586-023-06092-7
Son HA, Lee S, Lee J (2020) Numerical analysis of drag force acting on 2D cylinder immersed in accelerated flow. Water 12:1790
Suh S-H, Kim H-J, Jung W, Lee D-I (2024) The regional characteristics of raindrop size distribution by airflow conditions on Mountain Halla, a single bell-shaped mountainous area in South Korea. J Hydrometeorol 25:1525–1540. https://doi.org/10.1175/JHM-D-23-0087.1
Thomson RE, Gower JFR, Bowker NW (1977) Vortex streets in the wake of the Aleutian Islands. Mon Weather Rev 105:873–884
Wan R, Wu G (2007) Mechanism of the Spring Persistent Rains over southeastern China. Sci China Ser D Earth Sci 50:130–144. https://doi.org/10.1007/s11430-007-2069-2
Wang X, Alben S (2015) The dynamics of vortex streets in channels. Phys Fluids 27:528
Wang B, Wu R, Fu X (2000) Pacific-East Asian Teleconnection: how does ENSO affect East Asian climate? J Clim 13:1517–1536
Wang S, Hou Y, Zhou S, Zuo H, Sun F, Luo J-J (2021) Effect of circulation variation associated with East Asian jet on spring rainfall over North China and Yangtze-Huaihe River Valley. Atmos Res 258:105611. https://doi.org/10.1016/j.atmosres.2021.105611
Wheeler M, Kiladis GN (1999) Convectively coupled equatorial waves: analysis of clouds and temperature in the Wavenumber–Frequency Domain. J Atmos Sci 56:374–399
Wu R (1999) Principles of modern synoptic meteorology. Higher Education Press, Beijing (**(In Chinese)**)
Wu R, Hu Z-Z, Kirtman BP (2003) Evolution of ENSO-related rainfall anomalies in East Asia. J Clim 16:3742–3758
Wu Y et al (2024) Rising rainfall intensity induces spatially divergent hydrological changes within a large river basin. Nat Commun 15:823. https://doi.org/10.1038/s41467-023-44562-8
Xie S-P, Hu K, Hafner J, Tokinaga H, Du Y, Huang G, Sampe T (2009) Indian Ocean Capacitor Effect on Indo-Western Pacific climate during the summer following El Niño. J Clim 22:730–747. https://doi.org/10.1175/2008JCLI2544.1
Xie Z, Du Y, Yang S (2015) Zonal extension and retraction of the Subtropical Westerly Jet Stream and evolution of precipitation over East Asia and the Western Pacific. J Clim 28:6783–6798. https://doi.org/10.1175/JCLI-D-14-00649.1
Xie F, Ma X, Li J, Tian W, Ruan C, Sun C (2020) Using observed signals from the Arctic stratosphere and Indian Ocean to predict April–May precipitation in central China. J Clim 33:131–143
Yang F, Lau KM (2004) Trend and variability of China precipitation in spring and summer: linkage to sea-surface temperatures. Int J Climatol 24:1625–1644. https://doi.org/10.1002/joc.1094
Yeh T-C (1950) The circulation of the high troposphere over China in the winter of 1945–46. Tellus 2:173–183. https://doi.org/10.1111/j.2153-3490.1950.tb00329.x
Yeh TC, Gao Y (1979) Tibet plateau meteorology. Science, Beijing (**(In Chinese)**)
You Y, Jia X (2018) Interannual variations and prediction of spring precipitation over China. J Clim 31:655–670
Zhang Y, Guo L (2005) Relationship between the simulated East Asian westerly jet biases and seasonal evolution of rainbelt over eastern China. Chin Sci Bull 50:1503–1508. https://doi.org/10.1360/982004-361
Zhang R, Sumi A (2002) Moisture circulation over East Asia during El Niño episode in northern winter, spring and autumn. J Meteorol Soc Jpn Ser II 80:213–227